Journal of Power Sources 211 (2012) 97–102

Contents lists available at SciVerse ScienceDirect

Journal of Power Sources

journal homepage: www.elsevier.com/locate/jpowsour

Thermal dynamics and optimization on solid-state reaction for synthesis of Li_2MnSiO_4 materials

K. Gao [a], Chang-Song Dai [b], Jing Lv [a], Shu-Dan Li [a,*]

[a] School of Chemistry and Materials Science, Shanxi Normal University, Linfen 041004, China
[b] Department of Applied Chemistry, Harbin Institute of Technology, Harbin 150001, China

ARTICLE INFO

Article history:
Received 1 December 2011
Received in revised form
7 January 2012
Accepted 28 March 2012
Available online 12 April 2012

Keywords:
Solid-state reaction
Manganese silicate
Thermal dynamics
Li-ion batteries

ABSTRACT

A step-sintering method for preparing lithium magnesium silicate (LMS, Li_2MnSiO_4) can produce better optimized-Li_2MnSiO_4 (O-LMS) with smaller aggregates, more homogeneous phase and better electrochemical performance compared with Li_2MnSiO_4 prepared by continuously raising the temperature during the thermal treatment used to form Li_2MnSiO_4. The formation of Li_2MnSiO_4 is accompanied by three endothermic peaks (>200 °C) whose activation energies are calculated to be 350.78, 117.16 and 227.59 kJ mol^{-1} respectively using Kissinger differential method. The cell with a step-sintered O-LMS cathode can retain 73.5% of the initial discharge capacities after the 15th cycles, whereas only 55.6% for the cell with a continuously sintered LMS cathode.

1. Introduction

Developing cheap, sustainable and safe cathode materials is a prime target for the next generation of rechargeable lithium batteries. Recently, lithium transition metal orthosilicates (Li_2MSiO_4, M = Fe^{2+} [1–6], Mn^{2+} [7–17], Co^{2+} [18,19], Ni^{2+} [20]), have been attracting much attention as promising new storage cathodes. Among these silicate family materials, Li_2MnSiO_4 is considered to have a more potential market value than other counterparts. The main reasons can be summarized as follows: (1) There are the high theoretical capacities over 300 mAh g^{-1}, if the transition metal ions can be oxidized and reduced reversibly from Mn^{2+} to Mn^{4+} [13]. (2) Li_2MnSiO_4 shows appropriate lithium extraction voltage (4.1 and 4.5 V *vs.* Li) [20], which can be more suitable for the current organic electrolytes. (3) The resources to prepare Li_2MnSiO_4 material are plentiful and clean.

So far, many efforts have been made by many researchers to make clear the phase and characteristics of Li_2MnSiO_4 materials. The various synthetic routes have been used to prepare this new cathode material, such as solid-state reaction [7,8], sol–gel [9–12], Pechini process [13,14], hydrothermal reaction [15,16], polyol method [17], microwave solvothermal synthesis [21]. These works show that both the phase structure and the electrochemical performance of Li_2MnSiO_4 are dependent on synthesis conditions. Liquid-phase routes can usually produce the desired particulate morphologies with a good stoichiometry when compared with solid-state approaches. However, whatever method is used, the temperature rising and the high-temperature roasting are essential to prepare Li_2MnSiO_4. To our best knowledge, as for the thermal dynamics relevant to the synthesis of Li_2MnSiO_4, there are few reports addressing this issue until now. In the present study, to further understand solid-state reaction during preparing Li_2MnSiO_4, the synthetic process was analyzed by thermogravimetry–differential scanning calorimetry (TG–DSC) and Fourier transform infrared spectroscopy (FTIR). Based on the thermal dynamic results, an optimized step-sintering method was proposed to prepare Li_2MnSiO_4. Subsequently, the structure, morphology and electrochemical performance of optimized-Li_2MnSiO_4 were further investigated.

2. Experimental

According to the chemical formula of Li_2MnSiO_4, stoichiometric amount of SiO_2 (Henan Huanyu Power Source Co., Ltd), $LiCH_3COO{\cdot}2H_2O$ and $Mn(CH_3COO)_2{\cdot}4H_2O$ (Tianjin Guangfu Fine Chemical Research Institute) were ground to fine powder together with a agate mortar and pestle. The resulting intimate mixtures were used as the starting precursors.

* Corresponding author. Tel.: +86 357 2051192; fax: +86 357 2092341.
E-mail address: lishudan0451@163.com (S.-D. Li).

0378-7753/$ – see front matter © 2012 Elsevier B.V. All rights reserved.
doi:10.1016/j.jpowsour.2012.03.048

The thermogravimetry–differential scanning calorimetry (TG–DSC) measurements of the starting precursors about 15–25 mg were performed on a simultaneous thermal analyzer (TGA/DSC 1/1600, Switzerland Mettler-Toledo) from room temperature to 1000 °C under a nitrogen atmosphere at different heating rates of 5, 10, 15, 20 °C min^{-1}. FTIR spectra of the thermal treated precursors were collected using a Fourier transform interferometer (Model 640 America Varian) in the wave number region between 4000 and 400 cm^{-1}.

To prepare Li_2MnSiO_4/C materials, the starting precursors (80wt.%) and glucoses (20wt.%) were intimately mixed together, and then heated from room temperature to 700 °C for 10 h in a vacuum tube furnace keeping −0.1 MPa throughout. The optimized step-sintering method could be described as follows: the stoichiometric precursors were first heated to 200 °C and stayed for 2 h. Then, after milling and compacting, the obtained mixture was again transferred into vacuum tube furnace and successively calcinated at 400 °C for 3 h, 500 °C for 2 h, 700 °C for 10 h.

Powder X-ray diffraction (XRD, D8 Advance, Germany Bruker) employing Cu K_{a1} radiation ($\lambda = 1.5406$ Å) was used to identify the crystalline phase of final products. The morphologies were observed using a field-emission scanning electron microscope (FESEM, JSM-7500F, Japan JEOL) equipped with an energy dispersive spectroscopy (EDS, OXFOXD INCA PentaFET ×3). The Li/Mn ratio was determined using an inductively coupled plasma – atomic emission spectrometer (ICP-AES, OPTIMA 2100DV, America Perkin Elmer).

To prepare the tested positive cathodes, Li_2MnSiO_4/C materials (80wt.%), acetylene black (10wt.%) and polyvinylidene fluoride (10wt.%) were intimately mixed together. Then the N-methylpyrrolidone (NMP) as binder solvent was added to the above mixture with a proportion of 2.4 ml g^{-1}. After magnetic stirring for 10 h, the resulting slurry was coated onto an aluminum current collector and dried under vacuum at 100 °C for 12 h. Subsequently, the dry strip cathodes were cutting into the disks (16 mm in diameter) containing 8–12 mg Li_2MnSiO_4/C materials, in which the carbon content is about 11wt.% determined from TG data. The tested Li_2MnSiO_4/Li coin cells were fabricated in an Ar-filled glove box. One molar $LiPF_6$ – EC/DMC (1:1 by volume) was used as the electrolyte. Charge–discharge performance was characterized on a 5 V/2 mA battery testing system (Land 2005A, China Wuhan Jinnuo Electronics Co., Ltd.) with cut-off voltage of 1.5–4.5 V under a constant current density of 10 mA g^{-1}. The specific capacities were calculated based on the net mass of Li_2MnSiO_4 in the electrode.

3. Results and discussion

3.1. TG–DSC

As shown in Fig. 1, the typical TG curve is clearly separated by two main weight loss stages. This initial weight loss (24.58%) can be related to water removal, which is close to the theoretical value of 28.29% calculated from dehydrated reactions of the starting precursors. The second stage shows a sharp weight loss from 200 to 450 °C. Note the corresponding DTG curve shows two peaks, which implies there could be two main decomposition reactions occurring during this stage.

In Fig. 2, the DSC curves obtained at four different heating rates (5, 10, 15, 20 °C min^{-1}) are almost similar. There are five endothermic peaks in each curve, and the maximal temperatures (T_m) of these peaks increase slightly with an increase in the heating rate. The first two endothermic peaks can be assigned to the thermal dehydration and the fusion of $Mn(CH_3COO)_2$ (mp. 180 °C). The remaining three endothermic peaks appear in the range of

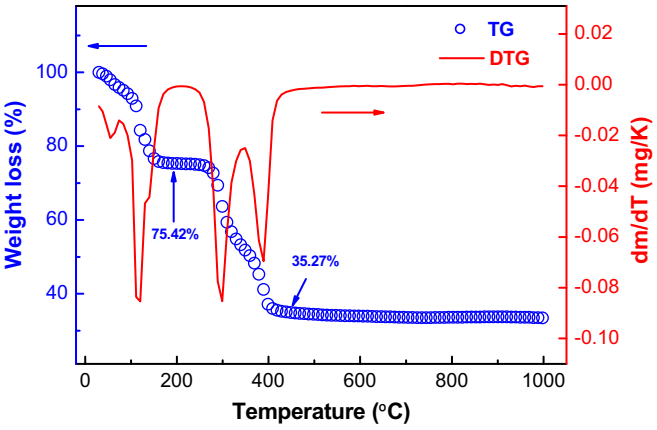

Fig. 1. Typical TG–DTG curve of Li_2MnSiO_4 precursors measured at a heating rate of 5 °C min^{-1}.

200–450 °C, and are called Peaks I, II and III in sequence. Peak I in the range of 227.01–270.48 °C with minor mass loss (about 1.36%), may mainly arise from the fusion of $LiCH_3COO$ (mp. 283–285 °C), possibly include the trace crystal water loss or some side reactions. Accordingly, Peak II and Peak III in the higher temperature range can be mainly attributed to the decomposition of the acetates. Thereafter, no noticeable thermal events are observed in DSC curves, we speculate the main formation reaction of Li_2MnSiO_4 may be included in the stage of Peak III.

3.2. FTIR

To further clear the details of thermal reactions during preparing Li_2MnSiO_4, the samples treated at different temperature are characterized by FTIR. The collected spectra are presented in Fig. 3 (2000–400 cm^{-1} region). Curve (a) and curve (b) show the characteristics of the dehydrated precursors. The main absorption features can be related to ν_{as}(C=O) at 1570 cm^{-1} and ν_s(C=O) at 1423 cm^{-1} from carboxylates [22], ν_{as}(Si–O–Si) at 1117 cm^{-1} and δ_s(Si–O–Si) at 474 cm^{-1} from SiO_2 [23]. It is noted that the separation between ν_{as}(C=O) and ν_s(C=O) is $\Delta\nu = 147$ cm^{-1} (<200 cm^{-1}), which means the formation of bridging bidentate acetate ligands (—C(O—Mn)(O—Mn)) matching to the IR bands at 662 and 621 cm^{-1} [24]. As for curve (c), the decrease in carboxylates

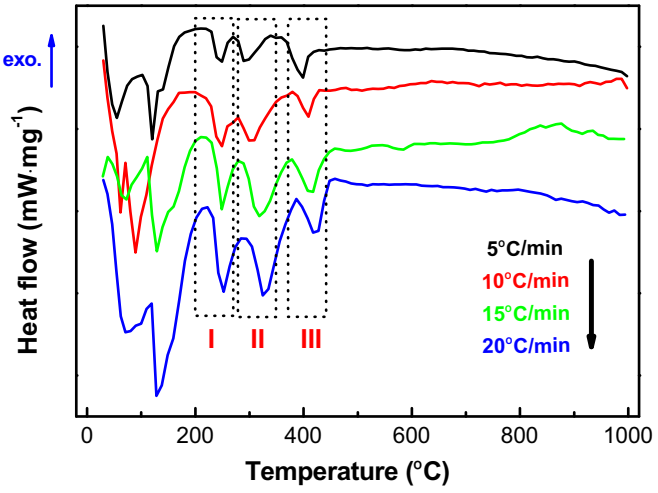

Fig. 2. DSC curves of Li_2MnSiO_4 precursors measured at different heating rates.

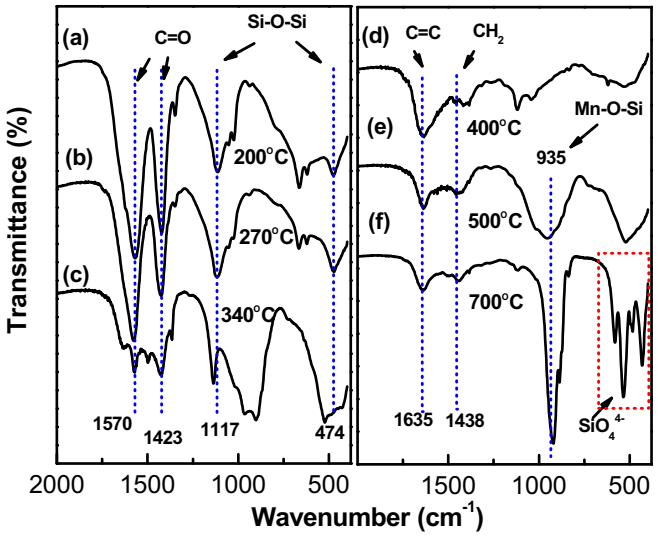

Fig. 3. FTIR spectra of the precursors calcinated at (a) 200 °C for 4 h, (b) 270 °C for 4 h, (c) 340 °C for 4 h, (d) 400 °C for 3 h, (e) 500 °C for 2 h, (f) 700 °C for 10 h.

intensities and the disappearance of O–Mn coordination bond mainly result from the decomposition of manganese acetate. The broadband from 900 to 1000 cm^{-1} infers that the main decomposition product is MnO in this stage. From curve (d), the spectral features of carboxylates disappear and the absorptions of O–Si–O move from the original wave number, which suggest that the formation of Li–Si–O intermediate products at Peak II step. For curve (e) and curve (f), it is worth to note that a new band appears at around 935 cm^{-1}, which has been assigned to a stretching vibration of Si–O–Mn linkage by many researchers [25,26]. So it is believed that Mn ions should have been incorporated into the framework of Si–O band in this stage. This result proves that the main solid reaction of Li_2MnSiO_4 formation should have been completed in Peak III zone. Additionally, compared with the broadband of the other curves in 400–600 cm^{-1}, the curve (f) shows a quiet clear outline of absorption peaks. These adsorption bands can be assigned to the fine structure of silicate tetrahedra (SiO_4^{4-}), mainly including out-of-plane bending vibration (ν_4 SiO_4^{4-}) at 525 cm^{-1}, the in-plane bending vibration (ν_2 SiO_4^{4-}) at 452 cm^{-1} and Si–O–Si bending vibrations centered around 620 cm^{-1} [27]. It is well-known that the adsorption bands in the IR spectra of an amorphous material are wider than those of the corresponding material in the crystal form [28]. This distinct difference in curve shape indicates the formation of crystal Li_2MnSiO_4 after calcination at 700 °C for 10 h.

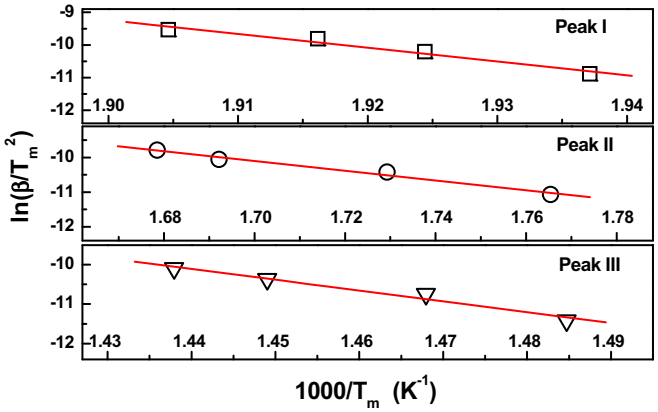

Fig. 4. Plots of ln (β/T_m^2) *vs.* $1000/T_m$ for Peaks I, II, III.

3.3. Thermal dynamics

The Kissinger differential method has been widely utilized to estimate the activation energy of reaction with its advantage not requiring any detailed information on the reaction mechanism [29–31]. The Kissinger's equation takes the form: $\ln(\beta/T_m^2) = C - (E/R)\cdot(1000/T)$, where E is the activation energy (kJ mol^{-1}), T_m the maximal temperature (K), β the heating rate (K min^{-1}), R the gas constant and C is a constant. The slope of $\ln(\beta/T_m^2)$ *vs.* $1000/T_m$ plot allows one to evaluate the activation energy. According to DSC data, the plots of $\ln(\beta/T_m^2) - 1000/T_m$ are displayed in Fig. 4 and the relevant thermal experiment data and linear fitting results are shown in Table 1. The activation energy was calculated to be 350.78 kJ mol^{-1} for Peak I, 117.16 kJ mol^{-1} for Peak II and 227.59 kJ mol^{-1} for Peak III respectively. Based on the results, it can be seen that Peak I had highest activation energy. That is to say, compared with Peak II and Peak III, Peak I is the most difficult step in the heating process. A possible reason is Peak I may involve more stages such as the fusion of acetates, the removal of trace water, the diffusion of molten materials and some side reactions, and so on. The deficient contact and slow diffusion in the multiphase systems may cause this result. It is well-known that the increase of reaction temperature or heating time should be favorable to the endothermic reaction. Therefore, based on the results, the optimized step-sintering method was used to prepare Li_2MnSiO_4. To test the efficacy of the new way, the subsequent discussion will be focused on the

Table 1
Thermal experiment data and fit linear results according to DSC curves.

Peak no.	T_m (°C)	$1/T_m \times 10^3$ (K^{-1})	β (°C min^{-1})	$\ln(\beta/T_m^2)$	$y = A + Bx$	R	E_a (kJ mol^{-1})
I	243.23	1.9371	5	−10.8837	$A = 70.9247$	−0.9840	350.78
	246.64	1.9244	10	−10.2037			
	248.88	1.9162	15	−9.8068	$B = -42.1911$		
	252.04	1.9046	20	−9.5312			
II	293.44	1.9371	5	−11.0693	$A = 13.8542$	−0.9914	117.16
	305.27	1.9244	10	−10.4175			
	317.96	1.9162	15	−10.0555	$B = -14.0915$		
	322.76	1.9046	20	−9.7839			
III	400.53	1.7654	5	−11.4156	$A = 29.3087$	−0.9871	227.59
	408.22	1.7293	10	−10.7452			
	417.12	1.6922	15	−10.3657	$B = -27.3743$		
	422.45	1.6785	20	−10.0934			

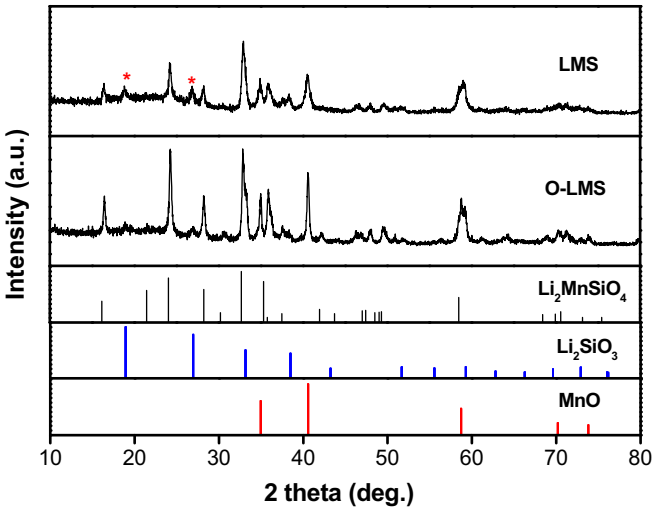

Fig. 5. Comparison and analysis of XRD patterns for LMS and O-LMS.

structure, morphology and electrochemical performance of Li_2MnSiO_4 (LMS) and optimized-Li_2MnSiO_4 (O-LMS).

3.4. XRD

The X-ray diffraction patterns of LMS and O-LMS are shown in Fig. 5. It can be seen that the positions of main peaks are almost similar for the both samples. Most of peaks can be assigned to Li_2MnSiO_4 phase. A few MnO impurities can be detected in both cases, in agreement with other reports [7,10,12,13]. It should be noticed that the stronger peaks around $2\theta = 19^\circ$ and 27° can be easily observed in the pattern of LMS sample, which can be related to certain distinguishable characteristics of Li_2SiO_3 phase. Moreover, the existed broad peaks indicate that in neither case the crystallinity is good, but the O-LMS sample shows the higher and sharper peaks. According to the Scherrer's equation, the mean crystallite size is calculated to be 13.4 nm and 23.3 nm for LMS and O-LMS respectively. The results prove that the optimized step-sintering method can facilitate forming crystal Li_2MnSiO_4.

3.5. SEM-EDS and ICP-ACS

As shown in Fig. 6, the both samples show irregularly-shaped aggregates composed of nanometer-sized primary particles (10–100 nm). Compared with LMS, the O-LMS shows smaller aggregated size no more than 5 μm (Fig. 6b). However, the former seems to show looser morphology with many voids (Fig. 6c). The observed results can be attributed to theirs different roasting process. In our experiments, the solid-state reactions should be accompanied with the release of gases due to the dehydration and decompositions of the precursors. Especially, for continuous rising temperature, due to uncontrollable heating temperature, it usually leads to the products with bigger aggregates and looser morphologies. Instead, to a certain extent, the optimized step-sintering method can suppress the overlapping degree of thermal reactions and allow the involved reactions to proceed more completely step by step.

The data of EDS and ICP-AES are shown in Table 2. By EDS spot (A and B) and mapping (C) analysis, we have been able to roughly determine the homogeneity of chemical elements. Here it should be point out that the unreasonable C and O content values can be attributed to the applications of conductive tapes in tested samples. The carbon content in samples can be determined to be around

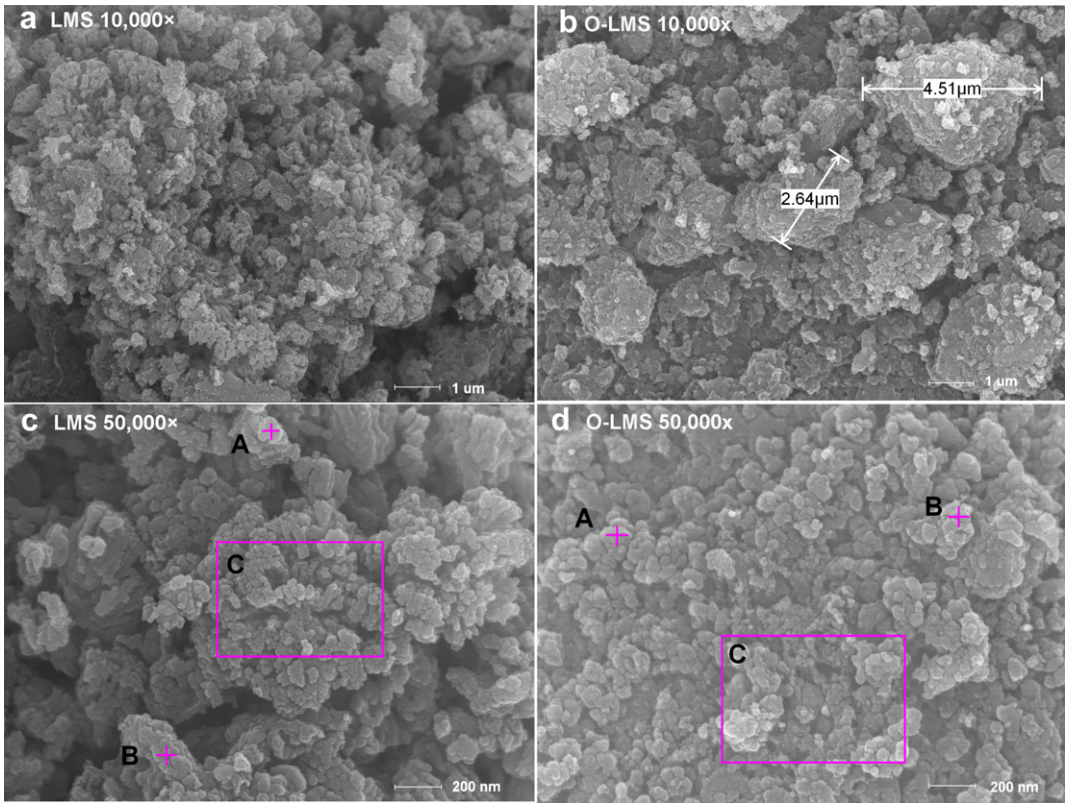

Fig. 6. SEM photographs of original magnification 10,000× and 50,000× for LMS and O-LMS.

Table 2
Summary of EDS and ICP-ACS data of LMS and O-LMS.

Element	EDS (atomic%)						ICP (mg/L)	
	LMS			O-LMS			LMS	O-LMS
	A	B	C	A	B	C		
Li	–	–	–	–	–	–	6.323	6.571
Mn	14.03	12.93	14.62	7.82	8.53	8.36	27.567	27.025
Si	20.65	15.20	14.89	7.68	7.96	8.41	Li/Mn = 1.82	Li/Mn = 1.93
C	30.24	36.64	36.00	42.98	44.27	41.53	–	–
O	35.09	35.23	34.50	41.52	39.24	41.69	–	–

11wt.% from TG data. By comparison, the O-LMS sample has very slight variation in the Mn/Si atomic ratios and shows more uniform element distribution than the LMS sample. Moreover, the ICP-ACS experiment indicates that the both samples are Li-defect compounds. It can be attributed to the evaporation of lithium compound during the roasting process, which is coincided with Jang's study on $LiCoO_2$ [32] and Guo's study on $Li_2Fe_{1-x}Mn_xSiO_4$ [33]. Therefore, this result suggests that a little more lithium in the precursors than the stoichiometric amount can compensate for lithium loss. It is obvious that, compared with O-LMS sample, the LMS sample has a larger deficiency in Li content, and the atomic ratio of Li/Mn is determined to be only 1.82 from ICP-ACS data.

3.6. Electrochemical performance

Fig. 7 shows a comparison of the electrochemical performance of LMS/Li and O-LMS/Li cells at room temperature. It can be seen that the initial charge capacities are 146.5 mAh g^{-1} for LMS cell and 201.8 mAh g^{-1} for O-LMS cell, corresponding to the exaction of 0.88 and 1.21 Li^+ per unit formula respectively. Besides charge voltage no more than 4.5 V, the Li deficiency in materials may be also responsible for the low amount of Li^+ exaction. It can be also seen that the charge curve in the first cycle is different from the charge curves in the following cycles. This fact has been investigated and reported by many other research groups [9,14] and they all agree that this phenomenon is cause by significantly structural changes (usually amorphism). It can be also estimated that the cell with O-LMS cathode can retain 73.5% of the initial discharge capacities after the 15th cycles, whereas only 55.6% for the cell with LMS cathode. Obviously, the optimized process cannot effectively hamper the Li_2MnSiO_4 crystal structure destruction. But, on the whole, the cells with O-LMS cathode have the higher discharge capacity and better capacity retention than that with LMS cathode. The improved cell performance can be ascribed to the smaller aggregates, higher-purity and better homogeneity of O-LMS materials.

4. Conclusion

In the present study, the TG–DSC and FTIR experiments infer that the main reaction of Li_2MnSiO_4 should be completed before 450 °C. By Kissinger differential method, the apparent activate energies of three endothermic peaks (>200 °C, Peaks I, II and III) are calculated to be 350.78, 117.16 and 227.59 kJ mol^{-1} respectively. The optimized step-sintering method is favorable to improving the qualities of Li_2MnSiO_4 materials. Benefiting from smaller aggregates, higher-purity and better homogeneity, the better electrochemical performance of O-LMS is confirmed by the contrast charge–discharge experiments. However, the optimized process cannot effectively hamper crystal structure destruction. To obtain high quality Li_2MnSiO_4 cathode materials, the other modified approaches, such as doping alien cations, should be specially considered in the future material design.

Acknowledgments

This work was financially supported by Research Fund for the Doctoral Program of Higher Education (grant no. 20101404120001)

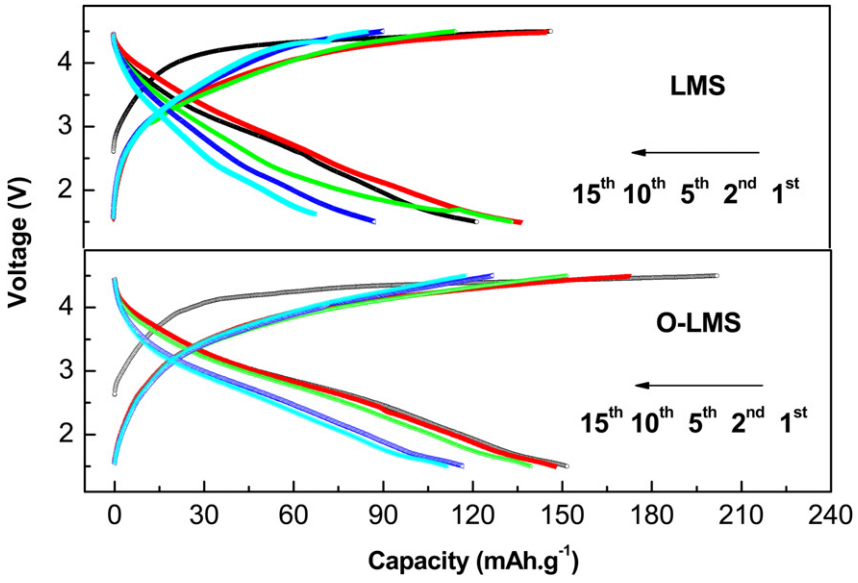

Fig. 7. Typical charge–discharge curves of the LMS/Li and O-LMS/Li cells.

and Supported by China Postdoctoral Science Foundation (grant no. 20110491051).

References

[1] A. Nytén, A. Abouimrane, M. Armand, T. Gustafsson, J.O. Thomas, Electrochem. Commun. 7 (2005) 156–160.
[2] R. Dominko, D.E. Conte, D. Hanzel, M. Gaberscek, J. Jamnik, J. Power Sources 178 (2008) 842–847.
[3] L.M. Li, H.J. Guo, X.H. Li, Z.X. Wang, W.J. Peng, K.X. Xiang, X. Cao, J. Power Sources 189 (2009) 45–50.
[4] K.C. Kam, T. Gustafsson, J.O. Thomas, Solid State Ionics 192 (2011) 356–359.
[5] S. Zhang, C. Deng, B.L. Fu, S.Y. Yang, L. Ma, Electrochim. Acta 55 (2010) 8482–8489.
[6] X. Huang, X. Li, H. Wang, Z. Pan, M. Qu, Z. Yu, Solid State Ionics 181 (2010) 1451–1455.
[7] W. Liu, Y. Xu, R. Yang, J Alloy Compd. 480 (2009) L1–L4.
[8] K. Karthikeyan, V. Aravindan, S.B. Lee, I.C. Jang, H.H. Lim, G.J. Park, M. Yoshio, Y.S. Lee, J. Power Sources 195 (2010) 3761–3764.
[9] Y.X. Li, Z.L. Gong, Y. Yang, J. Power Sources 174 (2007) 528–532.
[10] Ilias Belharouak, A. Abouimrane, K. Amine, J. Phys. Chem. C 113 (2009) 20733–20737.
[11] C. Deng, S. Zhang, B.L. Fu, S.Y. Yang, L. Ma, Mater. Chem. Phys. 120 (2010) 14–17.
[12] V. Aravindan, S. Ravi, W.S. Kim, S.Y. Lee, Y.S. Lee, J Colloid Interf. Sci. 355 (2011) 472–477.
[13] R. Dominko, M. Bele, M. Gaberscek, A. Meden, M. Remskar, J. Jamnik, Electrochem. Commun. 8 (2006) 217–222.
[14] R. Dominko, M. Bele, A. Kokalj, M. Gaberscek, J. Jamnik, J. Power Sources 174 (2007) 457–461.
[15] R. Dominko, J. Power Sources 184 (2008) 462–468.
[16] Z.L. Gong, Y.X. Li, Y. Yang, Electrochem. Solid-State Lett. 11 (2008) A60–A63.
[17] W. Liu, Y. Xu, R. Yang, Rare Met. 29 (2010) 511–514.
[18] Z.L. Gong, Y.X. Li, Y. Yang, J. Power Sources 174 (2007) 524–527.
[19] A. Robert Armstrong, Christopher Lyness, Michel Menetrier, Peter G. Bruce, Chem. Mater. 22 (2010) 1892–1900.
[20] M.E. Arroyo-de Dompablo, M. Armand, J.M. Tarascon, U. Amador, Electrochem. Commun. 8 (2006) 1292–1298.
[21] T. Muraliganth, K.R. Stroukoff, A. Manthiram, Chem. Mater. 22 (2010) 5754–5761.
[22] P. Roonasi, X. Yang, A. Holmgren, J. Colloid Interf. Sci. 343 (2010) 546–552.
[23] H. Pérez, P. Navarro, J. José Delgado, M. Montes, Appl. Catal., A Gen. 400 (2011) 238–248.
[24] T. Ivanova, A. Harizanova, Solid State Ionics 138 (2001) 227–232.
[25] L.Z. Wang, J.L. Shi, J. Yu, D.S. Yan, Nanostruct. Mater. 10 (1998) 1289–1299.
[26] M. Selvaraj, P.K. Sinha, K. Lee, I. Ahn, A. Pandurangan, T.G. Lee, Microporous Mesoporous Mater. 78 (2005) 139–149.
[27] O.E. Omotoso, D.G. Ivey, R. Mikula, J. Hazard. Mater. 42 (1995) 87–102.
[28] J. Lin, D.U. Sanger, M. Mennig, K. Barner, Thin Solid Films 360 (2000) 39–45.
[29] H.E. Kissinger, Anal. Chem. 29 (1957) 1702–1705.
[30] P. Zhang, X. Li, Z. Luo, X. Huang, J. Liu, Q. Xu, X. Ren, X. Liang, J Alloy Compd. 467 (2009) 390–396.
[31] H. Liu, Y. Yang, J. Zhang, J. Power Sources 173 (2007) 556–561.
[32] S.W. Jang, H.Y. Lee, S.J. Lee, H.K. Baik, S.M. Lee, Mater. Res. Bull. 38 (2003) 1–9.
[33] H. Guo, X. Cao, X. Li, L. Li, X. Li, Z. Wang, W. Peng, Q. Li, Electrochim. Acta 55 (2010) 8036–8042.